Comparison of tropospheric NO_2 from in situ aircraft measurements with near-real-time and standard product data from OMI

E. J. Bucsela,[1,2,3] A. E. Perring,[4] R. C. Cohen,[4] K. F. Boersma,[5] E. A. Celarier,[2,6] J. F. Gleason,[2] M. O. Wenig,[2,3,7] T. H. Bertram,[4] P. J. Wooldridge,[4] R. Dirksen,[5] and J. P. Veefkind[5]

Received 16 April 2007; revised 7 February 2008; accepted 3 March 2008; published 29 May 2008.

[1] We present an analysis of in situ NO_2 measurements from aircraft experiments between summer 2004 and spring 2006. The data are from the INTEX-A, PAVE, and INTEX-B campaigns and constitute the most comprehensive set of tropospheric NO_2 profiles to date. Profile shapes from INTEX-A and PAVE are found to be qualitatively similar to annual mean profiles from the GEOS-Chem model. Using profiles from the INTEX-B campaign, we perform error-weighted linear regressions to compare the Ozone Monitoring Instrument (OMI) tropospheric NO_2 columns from the near-real-time product (NRT) and standard product (SP) with the integrated in situ columns. Results indicate that the OMI SP algorithm yields NO_2 amounts lower than the in situ columns by a factor of 0.86 (±0.2) and that NO_2 amounts from the NRT algorithm are higher than the in situ data by a factor of 1.68 (±0.6). The correlation between the satellite and in situ data is good (r = 0.83) for both algorithms. Using averaging kernels, the influence of the algorithm's a priori profiles on the satellite retrieval is explored. Results imply that air mass factors from the a priori profiles are on average slightly larger (~10%) than those from the measured profiles, but the differences are not significant.

Citation: Bucsela, E. J., et al. (2008), Comparison of tropospheric NO_2 from in situ aircraft measurements with near-real-time and standard product data from OMI, *J. Geophys. Res.*, *113*, D16S31, doi:10.1029/2007JD008838.

1. Introduction

[2] NO_2 is an important trace gas because of its role as a pollutant and its reactions involving other atmospheric species, notably ozone [*Crutzen*, 1970; *Chameides and Walker*, 1973]. NO_x ($NO + NO_2$) is a key player in the chemistry of the lower troposphere, where NO_x from automobile and industrial emissions catalyzes reactions that generate smog [e.g., *Penner et al.*, 1991; *Seinfeld and Pandis*, 1998]. NO_x is also important in middle and upper tropospheric ozone chemistry [e.g., *Murphy et al.*, 1993], where it is largely produced by lightning [e.g., *Ridley et al.*, 1996]. The lifetime of NO_x in the upper troposphere is longer than at ground level, and this enhances its potential for ozone production [*Liu et al.*, 1987; *Pickering et al.*, 1990; *DeCaria et al.*, 2005]. Satellite data have been used to constrain NO_x emissions inventories of industrial emissions, as well as biomass burning and lightning sources [*Martin et al.*, 2003]. Profile measurements of NO_2 can provide additional information about the altitude dependence of NO_x chemistry, which is not available from the total column amounts obtained by nadir-viewing satellites. The profile shapes, defined by the relative amounts of NO_2 at different pressure levels, are also important in satellite retrievals, since the retrieval algorithms generally rely on normalized a priori NO_2 profiles [*Martin et al.*, 2002; *Bucsela et al.*, 2006]. Such profiles have traditionally been obtained from chemical transport models (CTM) like GEOS-Chem [*Bey et al.*, 2001; *Martin et al.*, 2002b], but aircraft measurements of NO_2 can now be used to validate these profiles.

[3] Until recently, systematic measurements of NO_2 using airborne instruments have been scarce. *Heland et al.* [2002] measured in situ mixing ratios of NO_2 and used the resulting profile for the first comparison with a measurement of NO_2 from GOME. Although their analysis required some extrapolation of the measured profile in the boundary layer, their results were found to be relatively insensitive to the assumptions used in the extrapolation. The profile shape and integrated column amount obtained were consistent with GOME's retrieval algorithm and retrieved tropospheric NO_2 amount. *Heue et al.* [2005] used an airborne Multiaxis DOAS (AMAXDOAS) instrument to measure NO_2 around the Mediterranean and validate satellite measurements from the Scanning Imaging Absorption Spectrometer for Atmospheric Chartograpyy (SCIAMACHY) instrument on the

[1]SRI International, Menlo Park, California, USA.
[2]NASA Goddard Space Flight Center, Greenbelt, Maryland, USA.
[3]Goddard Earth Sciences and Technology Center, University of Maryland, Baltimore County, Baltimore, Maryland, USA.
[4]Department of Chemistry, University of California, Berkeley, California, USA.
[5]Royal Netherlands Meteorological Institute, De Bilt, Netherlands.
[6]SGT, Inc., Greenbelt, Maryland, USA.
[7]Department of Physics and Materials Science, City University of Hong Kong, Kowloon, Hong Kong.

Copyright 2008 by the American Geophysical Union.
0148-0227/08/2007JD008838

European ENVISAT. NO_2 profiles from in situ measurements during the summer of 2004 International Consortium for Atmospheric Research on Transport and Transformation/Intercontinental Chemical Transport Experiment (ICARTT/INTEX-A) campaign were analyzed by *Martin et al.* [2006], and compared to SCIAMACHY retrievals as well as the GEOS-Chem model.

[4] In this study, we examine averaged profiles from INTEX-A and the Polar Aura Validation Experiment (PAVE), as well as individual profiles from the second phase of the Intercontinental Chemical Transport Experiment (INTEX-B). We qualitatively compare these (INTEX-A and PAVE) to the a priori profiles employed in algorithms to retrieve tropospheric NO_2 from the Ozone Monitoring Instrument (OMI). Quantitative analysis with averaging kernels is used with the INTEX-B data to ascertain the effect of profile shape on the satellite retrieval. We also integrate the profiles from INTEX-B to produce tropospheric NO_2 column amounts, which we compare to coincident satellite measurements from OMI. The results are used to validate the methods used in the OMI algorithms and the retrieved tropospheric NO_2 amounts. We discuss our findings and their implications.

2. Data Description

[5] The data in this study consist of satellite remote sensing measurements from the Ozone Monitoring Instrument and in situ observations from instruments flown on the DC-8 aircraft. The majority of the observations presented here were obtained during the INTEX-B campaign, conducted in the spring of 2006. Additional measurements were made in the summer of 2004 during INTEX-A and the winter of 2005 during PAVE. The following is a brief overview of the instruments and data reduction algorithms used to process the measurements.

2.1. Aircraft Measurements

[6] The in situ data were obtained using the UC Berkeley Laser-Induced Fluorescence instrument (TD-LIF). The instrument and ground-based comparisons of the LIF technique with DOAS and photolysis-chemiluminescence instruments have previously been described in detail by *Thornton et al.* [2000, 2003]. Agreement among the three techniques was found to be better than 10%. Improvements have been made to the instrument for its implementation on the DC-8, including the use of a supersonic expansion to enhance sensitivity [*Cleary et al.*, 2002]. Further details and comparisons to other airborne instruments will be presented elsewhere (T. H. Bertram et al., manuscript in preparation, 2008). Here we provide a brief overview of the instrument and its operation. A Q-switched Nd:YAG laser (7 khz, 3 W, 532 nm) is used to pump a narrowband (0.06 cm^{-1}) tunable dye laser operating at 585 nm. The dye laser beam makes 32 passes through the core of a supersonic expansion which causes thermal cooling of the gas and thus increases the population of NO_2 molecules in the target rotational level [*Cleary et al.*, 2002]. The resulting red-shifted fluorescence is collimated and passed through filters to reject Raman and Rayleigh scatter, as well as most of the scatter from the walls of the chamber. The filtered radiation is then focused onto a photomultiplier (Hamamatsu H7421-50). Time gated photon counting techniques are used to increase the rejection of prompt scattering while collecting most of the long-lived fluorescence from NO_2. The dye laser frequency is alternately tuned between the peak absorption of a strong resonant feature (10 s) and an offline position in the weak continuum absorption (5 s). The difference between the two signals is directly proportional to the NO_2 mixing ratio.

[7] Data from the TD-LIF instrument were collected at 1-s intervals. At 1 Hz, the mixing ratio observations have precisions ranging from ±23 ppt at 1000 hPa to ±46 ppt at 200 hPa (S/N = 2). From these we estimate 1-min detection limits of 3 ppt at the ground and 6 ppt at 12 km. Ultrapure air was used to provide NO_x-free samples to calibrate the instrument and determine zeros. A zero was performed during each level leg at least once per hour. A 5 ppm Praxair NO_2 in N_2 tank (stated certainty to within 5%, confirmed by laboratory experiments) was used for calibration of the instrument during level flight at least once every 2 h. The tank was compared to a library of tanks of different ages and concentrations before and after the campaigns, and no appreciable drift was observed. More variability over time has been observed in mass flow controllers and regulators than in the tanks themselves, and stable tanks have been seen, through regular monitoring to remain so for years. An upward humidity correction of <10% was also applied to the data to account for the influence of water vapor on the fluorescence lifetime of NO_2. On the basis of known uncertainties in the reference calibration standard, the reproducibility of the calibrations in flight and the reproducibility of the measurements of the instrument zero, the NO_2 measurements are believed to be accurate to ±10% ± 5 ppt.

2.2. OMI Measurements

[8] The Ozone Monitoring instrument has been obtaining measurements of NO_2 and other trace gases every day beginning approximately two months after its launch on board the Aura satellite in July 2004 [*Levelt et al.*, 2006]. It provides daily global coverage with nadir resolutions of 13×24 km^2. This is a higher resolution than available from GOME or SCIAMACHY and allows identification of urban-scale pollution sources. The instrument and data analysis represent a joint venture between the Netherlands Royal Meteorological Institute (KNMI) and NASA Goddard Space Flight Center (GSFC) in the U.S. Two NO_2 data products are available from OMI, namely the standard product (SP) from GSFC and the near-real-time product (NRT) from KNMI. The two products employ the same spectral analysis, which yields NO_2 slant column densities (SCDs), but differ in the subsequent algorithms for separating the SCDs into stratospheric and tropospheric components and then converting them to vertical column densities (VCDs). Both algorithms apply a correction for the cross-track anomaly in the SCDs. The anomaly gives the appearance of stripes when the data are mapped. The algorithms use different methods for computing air mass factors (AMFs), which are defined as the ratio of SCD to VCD. Below are brief overviews of the algorithms.

[9] The algorithm used to create NO_2 standard product is described by *Bucsela et al.* [2006], *Wenig et al.* [2008] and *Celarier et al.* [2008]. The NO_2 slant columns are computed by fitting the OMI spectra using cross sections for NO_2 and

ozone, as well as a Ring spectrum to account for rotational Raman scattering. A full day of data (15 orbits) is obtained using data from within ±12 h of each OMI orbit to produce global coverage. The SCDs are divided by an AMF based on an a priori stratospheric NO_2 profile to yield initial vertical column densities. These initial VCDs are approximately equal to the total NO_2 vertical column over regions uncontaminated by tropospheric NO_2, since, by definition, most NO_2 in these regions is stratospheric [*Bucsela et al.*, 2006]. Locations in the initial VCD field where the mean annual tropospheric NO_2 column is greater than 0.5×10^{15} cm^{-2}, on the basis of a priori GEOS-Chem model information are masked. The remaining areas are used to generate a smoothed, interpolated stratospheric field using planetary wave-2 analysis in 9° wide zonal bands. Differences, ΔVCD, between the initial VCD field and this smoothed field are used to determine the presence of tropospheric NO_2 pollution. Where the differences are positive, the value of ΔVCD is corrected by multiplying it by the ratio of the stratospheric-to-tropospheric AMF. The tropospheric AMF is computed from an a priori geographically gridded set of annual mean tropospheric NO_2 profiles from the GEOS-Chem model. Surface albedos are from *Koelemeijer et al.* [2003]. The corrected ΔVCD gives an estimate of the "polluted" NO_2 amount, i.e., the amount of NO_2 in the lower to middle troposphere. Where ΔVCD is negative, this polluted amount is taken to be zero. Approximately 5% of the "stratospheric" column is assumed to be below the tropopause height, defined to be at the ~200 hPa pressure level, and this column is added to the polluted column to give the tropospheric NO_2 amount. In the case where the field of view contains clouds, the "below-cloud" amount from the data files must also be added to the tropospheric column amount to give the complete tropospheric column. The below-cloud is derived from the observations by effectively scaling the a priori profile shape to the observed ΔVCD, which is taken as the tropospheric NO_2 amount observed above the cloud. Addition of this amount to the SP data is equivalent to defining the tropospheric AMF as the ratio of the observed SCD divided by the complete tropospheric column between ground and tropopause. For cloud fractions less than 30%, this below cloud fraction is generally less than 20%, depending on pollution levels. The cloud parameters are obtained from the OMI O_2–O_2 cloud algorithm [*Acarreta et al.*, 2004].

[10] The near-real-time NO_2 data for a given location are released within 3 h of the time of satellite overpass. An in-depth description of the product is given by *Boersma et al.* [2007]. The NRT algorithm employs a more sophisticated approach to data processing that relies strongly on meteorological data and model output. NRT stratospheric NO_2 is derived through an assimilation technique in which measured slant columns are weighted according to their estimated degree of tropospheric contamination. The model employed is the global chemistry and transport model, TM4 [*van Noije et al.*, 2006]. Columns from relatively "clean" regions are used to constrain the TM4 stratospheric NO_2 amount, and stratospheric NO_2 in the remaining areas is computed by advection. This approach provides fine structure in the stratospheric NO_2 field not present in the standard product. Tropospheric AMFs are computed from TM4 NO_2 profiles for the time and location of the OMI overpass. Surface pressures are based on daily ECMWF estimates, which are on a coarser geographic grid than the climatological estimates used in the standard product. The surface albedos in the NRT algorithm are from a combination of the 5-year *Koelemeijer et al.* [2003] database, and the 13-year *Herman and Celarier* [1997] climatology. Surface albedos in the SP and NRT algorithms may differ by ±0.02 or more. As in the SP algorithm, cloud parameters for AMF calculations in the NRT algorithm are based on the cloud model of *Acarreta et al.* [2004]. The NRT algorithm applies a tropospheric AMF correction to ΔVCD for both positive and negative values.

3. Analysis

3.1. Profiles

[11] The Berkeley TD-LIF profile measurements were binned on a pressure grid. For the INTEX-B analysis, the grid was based on the same 25 pressure levels used in the OMI SP algorithms. Bins are centered on each of the 25 levels, with bin widths equal to the level spacing, which varies from 10 hPa near the ground, to 25–50 hPa in the middle and upper troposphere, to 80 hPa near the top of the profile at 200 hPa. This binning scheme maintains adequate signal-to-noise levels while capturing the vertical structure in the atmosphere, especially in the vicinity of the planetary boundary layer (PBL) where the mixing ratios exhibit steep gradients. Similar bin sizes near ground were used in the aircraft study of *Heland et al.* [2002]. A typical profile measurement contains on the order of 10^3 1-s-long measurements, resulting in ~40 measurements per bin. The median value in each bin was chosen as the NO_2 mixing ratio at that pressure. Medians rather than means were used as a robust estimate of the central value, since several bins contained apparent outliers. The random component of the uncertainty was taken to be the standard deviation of the data in a bin divided by the square root of the number of measurements in the bin.

[12] Integration of the INTEX-B column data required estimates of mixing ratios in bins where no aircraft measurements were available. The estimates depended on the locations of the "empty" bins. Mixing ratios in bins between those with valid measurements were found by linear interpolation in log-log space. Empty bins at the top of a given profile were replaced by a daily composite of flight measurements. Where the composite did not extend to 200 hPa, the annual mean GEOS-Chem profile for that geographic location was scaled to the measured profile's integrated column amount and used to extrapolate the top of the profile. Extrapolations at the bottoms of the profiles, which were generally larger, were based on the average of two methods. The first assumes a constant mixing ratio in the extrapolated segment. It weights the mixing ratio in the lowest measured bin most heavily. The second uses the local GEOS-Chem model profile, scaled to the entire measured column amount. This approach gives comparable weight to all measured bins but can create artificial discontinuities at the bottom of the profile. The average method represents a compromise between these approaches. The extrapolated segments of each column are estimated to have uncertainties corresponding to variation by a factor of 1.5–2.0. This is supported by a model study of GEOS-Chem output, which showed a similar range of lower

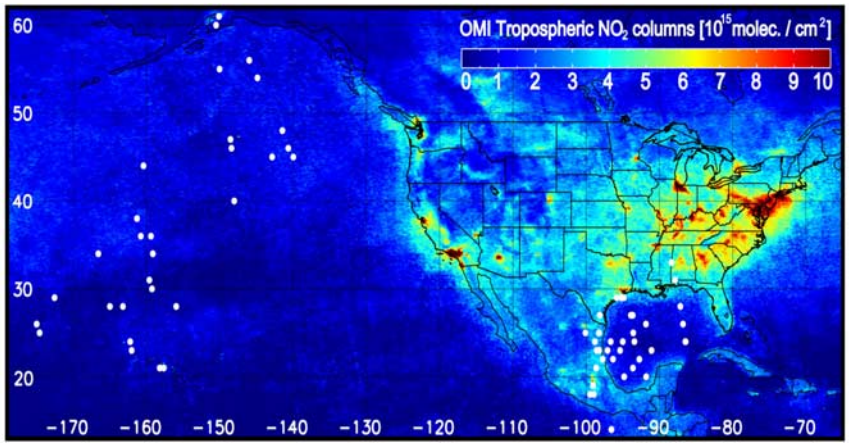

Figure 1. Mean tropospheric NO_2 amount from the OMI standard product averaged over 14 days of the INTEX-B campaign (March–May 2006). White dots show the locations of the 71 NO_2 profiles which were obtained on those days and used in this study.

tropospheric variability for a given month, location and free-tropospheric column amount. To facilitate error estimates for regression analyses (see section 4) we treat this uncertainty as an 80% relative error in the extrapolated column amount.

[13] The INTEX-B profiles were integrated above the NCEP monthly climatological surface pressures at the locations of the selected OMI pixels (see section 3.2). Since the pressures sometimes varied among the pixels associated with a given profile, the column amounts above the individual pixels were averaged to yield a single in situ column value, V_{in_situ} for the profile. For some of the pixels, the surface pressure was lower than the base of the profile. In those cases, the profile was shifted up to the surface pressure to preserve the same mixed layer height and mixing ratio. This effectively avoids diminution of the PBL thickness. This technique was especially important for profiles near Mexico City, where the terrain height is highly variable. The variability was also accounted for in the column error estimate. A piecewise linear variation of log mixing ratio versus log pressure was assumed between each of the binned mixing ratio values, and no ancillary temperature or height information was needed for the integrations. This approach yields accurate column densities, especially in regions where NO_2 concentrations decrease rapidly with height. Errors in the integrated columns were computed as the sum of uncertainties due to random error derived mainly from scatter in the measurements, and an additional 10% uncertainty to account for systematic error in the LIF measurements. This was combined with the uncertainty in the extrapolated column amount. We estimate a total column detection limit of 0.1×10^{15} cm^{-2}, based on the 1-min mixing ratio detection limits given in section 2. Where the computed uncertainty is less than this value, the uncertainty is clamped at the detection limit to prevent unrealistically small error estimates from biasing the statistical analysis.

3.2. OMI Data Selection for INTEX-B

[14] A total of 109 profiles were available from 14 days of the INTEX-B campaign between 4 March and 9 May 2006. A subset of these was integrated for comparison with tropospheric column amounts from a colocated subset of OMI pixels. Selection of profiles and OMI pixels were based on the following criteria:

[15] 1. The profile measurement must have been made within 3 h of OMI overpass, with at least two available OMI pixels containing a valid (nonfill value) tropospheric NO_2 measurement.

[16] 2. The OMI pixel centers must be within 0.2° of the nearest low-level aircraft measurement. We define a low-level measurement as one made while the aircraft was flying below the 500 hPa level.

[17] 3. The effective geometrical cloud fraction in the OMI pixels must be less than 30%.

[18] The thresholds for these criteria were set to balance data quality with a sufficient number of measurements for good statistics. Criterion 1 minimizes temporal variations in NO_2 near the profile measurement due to chemistry and transport. In 3 h, a 10 m/s wind transports air a distance of <5 OMI pixels. Criterion 2 includes only OMI pixels where the aircraft probed the lower troposphere, since the tropospheric signal is often dominated by boundary layer NO_2. Although flight restrictions limited aircraft measurements to altitudes above 150 m over water and 300 m over land, all but six of the profiles used in this study included some measurements made in the boundary layer. The portion of the NO_2 column below 500 hPa ranged from 20 to 50% for profiles over clean ocean regions, to >90% over polluted areas. The effective geometrical cloud fraction in criterion 3 is the fraction of opaque Lambertian clouds with an albedo of 80% that gives the observed cloud radiance, and is obtained from the OMI O_2-O_2 cloud product. The <30% threshold is equivalent to a <65% threshold on the fraction of radiance from the cloudy part of a pixel. Restrictions based on these combined criteria resulted in a total of 71 profiles for the SP data, as shown on the map in Figure 1. The statistics of the column fraction for these profiles obtained by extrapolation are plotted as a histogram in Figure 2. For the NRT data, a total of 58 profiles were found to match the selection criteria, with 20 of the profiles obtained over land in both cases. Fifty-three of the profiles matched the criteria for both data sets, which were somewhat different because of the availability of valid OMI measurements in each case.

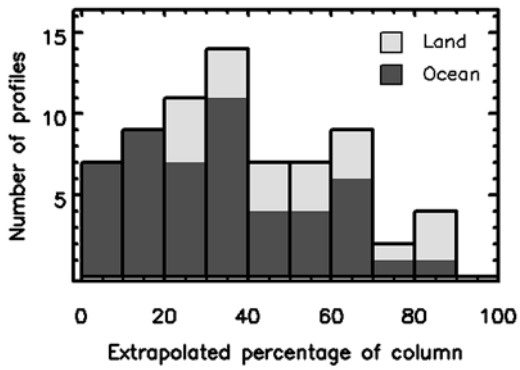

Figure 2. Statistics of the extrapolated fraction of the vertical column computed for the in situ profiles. Typically, land profiles required more extrapolation than those over water.

[19] The OMI column amounts were obtained from the level 2 data files for the NRT and standard products. The numbers of OMI pixels associated with a given profile ranged from 3 to 31. In the standard product, the "below-cloud" amount (described in section 2.2) was added to the tropospheric column. For each profile, the OMI tropospheric vertical column, V_{OMI}, is taken to be the average of the values for the individual pixels. The uncertainties are computed as the average of two estimates of the error for a single pixel, divided by the square root of the number of pixels. These two single-pixel error estimates are (1) an a priori estimate of the tropospheric column error for a single pixel using an approach similar to *Boersma et al.* [2004] and (2) the standard deviation of the pixel values. The estimates generally agree within a factor of two, and using either estimate alone to represent the OMI error does not significantly affect the results of this study. The single-pixel detection limit for all OMI data was estimated to be 0.5–1.0 $\times$ 10^{15} cm^{-2}. We use 0.7 $\times$ 10^{15} cm^{-2} divided by the square root of the number pixels as a lower bound on the OMI uncertainties.

[20] Figure 3 shows examples of NO_2 profiles and corresponding aircraft spirals from INTEX-B obtained in March 2006. For the profiles, Figures 3a and 3b, dots indicate individual aircraft measurements and the blue line shows the binned profile with error bars. Most of the scatter is due to the low precision of the individual measurements, which is improved by binning and accounted for in the error bars. The binned profile is thought to better reflect the ambient variability. Note that the largest error bars are associated with the extrapolated parts of the profile. The red line shows the scaled GEOS-Chem annual mean profile for the geographic location of the measured profile. The aircraft trajectories in Figures 3c and 3d have thick and thicker portions to indicate the locations of the plane while flying below 500 hPa and 900 hPa (the approximate top of the PBL), respectively. The small boxes marking the centers of the OMI pixels used in the comparison are color coded according to the OMI tropospheric column amount. The relatively wide areas covered by the OMI pixels helps reduce noise in the averaged column values. However, as Figures 3c and 3d show, the NO_2 field can be highly inhomogeneous, and the large values in the southern pixels in Figure 3c may be due to a real plume of enhanced NO_2. This potential plume is not represented in the aircraft measurements, which did not record the lower troposphere in this region. Spatial inhomogeneity can also affect individual pixels that cover a large area, such as those near the edges of the orbital swath. Because of their large viewing zenith angles, edge-of-swath pixels are also associated with large uncertainties in the NO_2 amounts, and these uncertainties are included in the calculation of the overall OMI uncertainty for a given profile. The majority ($\sim$2/3) of the profile measurements were made within 20° of nadir.

4. Results

4.1. INTEX-A and PAVE Profile Shapes

[21] Composite tropospheric NO_2 profiles measured during the INTEX-A and PAVE campaigns were compared with annual mean tropospheric NO_2 profiles from the GEOS-Chem model. The profiles are shown in Figure 4. The model profiles are the same as those used in the OMI NO_2 SP algorithm for AMF calculations and are chosen from arbitrary locations for this comparison. The composites are based on profiles collected during each campaign, and include summertime continental and Atlantic Ocean profiles from INTEX-A, and a continental wintertime profile from PAVE. It should be noted that many of the measurements over land, particularly during PAVE, were obtained upon descent into the airport and thus do not necessarily represent the overall continental profile. Nonetheless, comparisons with the models reveal that the measured profiles are qualitatively similar, but some differences are evident. Relative to the model profiles, the INTEX-A composites contain a larger proportion of NO_2 in the upper troposphere.

[22] The profile shapes, rather than their magnitudes, are important in the AMF calculations. Following *Palmer et al.* [2001], the tropospheric air mass factor, M, is computed a priori from the expression:

$$M = \frac{1}{V_a} \int_{zsurf}^{ztrop} \mathrm{d}z \cdot m(z) \cdot n_a(z) \tag{1}$$

where the $m(z)$ is a profile of altitude-dependent scattering weights [*Palmer et al.*, 2001; *Martin et al.*, 2003; *Bucsela et al.*, 2006], which are defined here to include the effect of NO_2 temperature on the amount of absorption, and $n_a(z)$ is the a priori (model) NO_2 number density profile. Here the profiles are defined at altitude, z, and integrated between surface altitude z_{surf} and tropopause altitude z_{trop}. In practice, the integrations are carried out in mixing ratio versus pressure space. The profiles are normalized to the a priori vertical column, V_a, which is related to $n_a(z)$ by the expression

$$V_a = \int_{zsurf}^{ztrop} \mathrm{d}z \cdot n_a(z) \tag{2}$$

[23] Clear-sky air mass factors are shown in Table 1 for the profiles in Figures 3 and 4. For the composite and corresponding model profiles, the AMFs were computed for average viewing conditions (solar zenith angle = 45°, viewing zenith angle = 10°, surface albedo = 0.05). In the summer example the AMFs based on the measurements are smaller than those computed from the model, but in most

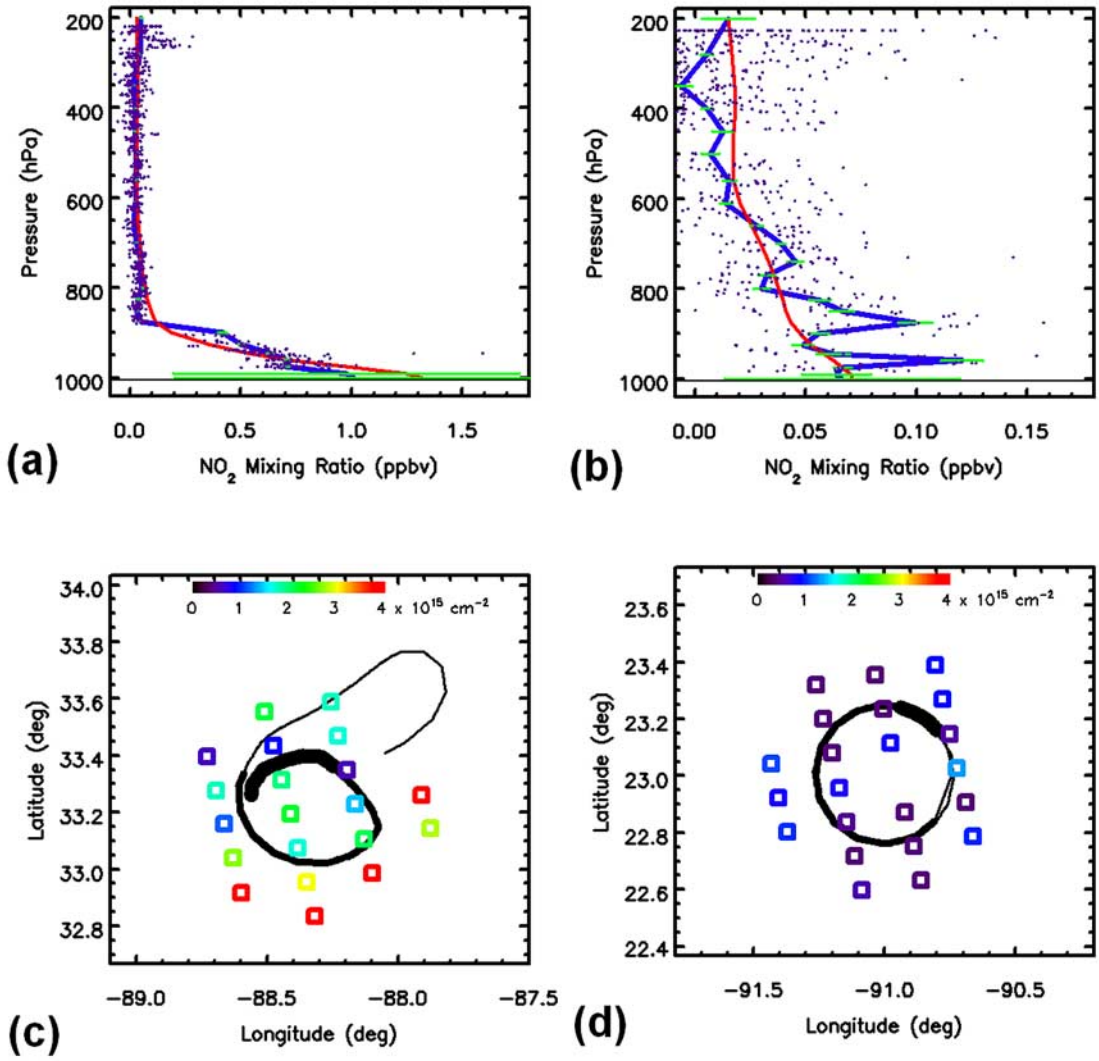

Figure 3. (a and b) Two INTEX-B NO_2 profiles, with (c and d) corresponding aircraft spirals. In Figures 3a and 3b, dots are original measurements, blue line is binned profile, and red line is annual mean GEOS-Chem model profile for that location. In Figures 3c and 3d, medium-thick line is for aircraft measurements below 500 hPa, and thick line is below 900 hPa. Colored boxes show centers and tropospheric column amounts for SP OMI pixels used in the comparison.

cases the differences are not large. These results are consistent with the findings of *Martin et al.* [2006] in their analysis of profiles from the ICARTT aircraft campaign over North America. They found AMFs from measured profiles that were 9% and 12% larger than coincident GEOS-Chem profiles for ocean and land measurements, respectively. *Martin et al.* [2006] and *Hudman et al.* [2005] have suggested that such differences may be due to deficiencies in lightning NO_x production in earlier versions of GEOS-Chem, such as the one used to generate profiles for the SP algorithm.

4.2. INTEX-B Column Comparisons

[24] Integrated in situ NO_2 columns from the INTEX-B campaign were compared with tropospheric columns from each of the two OMI NO_2 algorithms using linear regression. A chi-square minimization procedure was used to fit a straight line through the N data points with error bars in both coordinates [*Press et al.*, 1992]. In this method, each data point is assigned a weight equal to $1/(\acute{o}_y^2 + b^2 \cdot \acute{o}_x^2)$, where $\acute{o}_x$ and $\acute{o}_y$ are the respective uncertainties in the in situ and OMI columns, and b is the slope of the fitted line.

[25] Figure 5 compares the INTEX-B in situ and OMI column amounts, which we call V_{in_situ} and V_{OMI}, respectively. Here, V_{OMI} is the column amount from either algorithm, i.e., V_{OMI}(SP), or V_{OMI}(NRT). In Figure 5a, we plot V_{OMI}(SP) against V_{in_situ} for the 71 cases that met the SP selection criteria. The Pearson's correlation coefficient for the two sets of measurements is r = 0.83. The slope of the fitted line is 0.86 ± 0.11, which implies a small underestimation by OMI with respect to INTEX-B. The y intercept of 0.14 ± 0.05 × 10^{15} cm^{-2} indicates a small positive bias in the OMI data for small column amounts. The results of comparisons with the NRT data are shown in

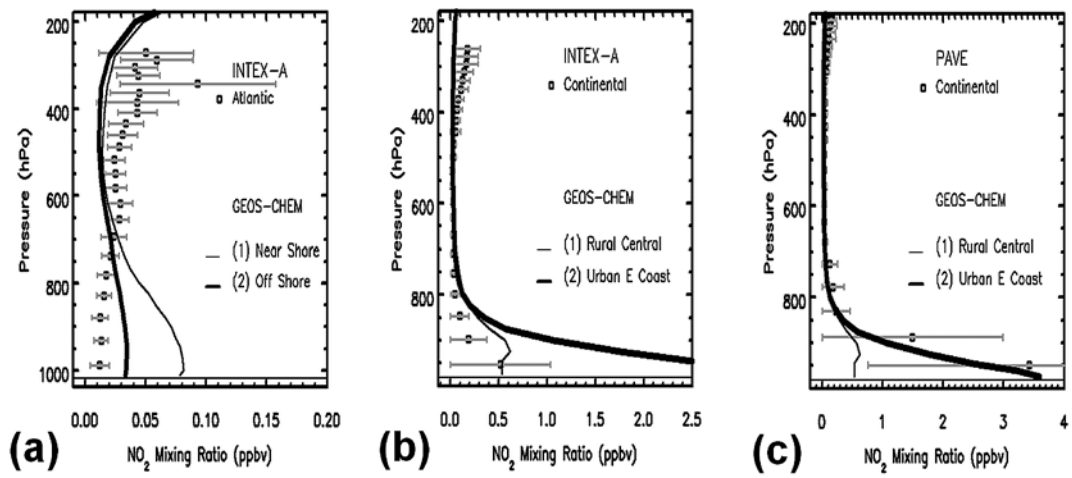

Figure 4. In situ profiles (boxes are means with error bars for the associated standard deviations) from the INTEX-A (summer) and PAVE (winter) campaigns, compared with GEOS-Chem model profiles (thin and thick lines): (a) INTEX-A Atlantic composite profile, (b) INTEX-A continental composite profile, and (c) PAVE continental composite profile. The continuous vertical curves are two arbitrary annual mean GEOS-Chem model profiles shown for comparison (see text and Table 1). Differences in the error bars in Figures 4a–4c reflect real differences in the variance of the data between the profiles.

Figure 5b, where V_{OMI}(NRT) versus V_{in_situ} are plotted using the 58 valid NRT cases. The correlation coefficient is the same, but the slope and intercept are 1.68 (±0.23), and −0.59 (±0.10) × 10^{15} cm^{-2}, respectively, indicating a larger negative bias for small columns and an overestimation for larger columns relative to INTEX-B.

[26] The slope and intercept uncertainties for both regressions assume random errors only. Consideration of systematic errors in the analysis leads to larger uncertainties in the fitted values. Some of the analysis errors are described in section 5. Taking these into account, we adopt the following estimate of the slope, intercept and corresponding uncertainties:

$$V_{OMI}(\mathrm{SP}) \text{ versus } V_{in_situ} : \text{Slope} = 0.86\ (\pm 0.2)$$
$$y \text{ intercept} = 0.14\ (\pm 0.1) \times 10^{15}\ \mathrm{cm}^{-2}$$
$$V_{OMI}(\mathrm{NRT}) \text{ versus } V_{in_situ} : \text{Slope} = 1.68\ (\pm 0.6)$$
$$y \text{ intercept} = -0.59\ (\pm 0.2) \times 10^{15}\ \mathrm{cm}^{-2}$$

[27] Besides the correlation coefficient, it is useful to investigate the statistical significance of the difference between the in situ measurements and OMI measurements. The paired t test indicates whether the difference is significantly different from zero, given the variance in the two data sets. We find that both the near-real-time and standard product give paired t statistics that are smaller than the critical t values at the 95% confidence interval. For the SP data, $t = 1.23$, and for the NRT data $t = 0.38$. These values are smaller than t-critical, which is 1.67 for both data sets. Thus, for the observed variances, the differences between the in situ and corresponding satellite measurements are not significant.

[28] Figure 6a is a comparison of V_{OMI}(NRT) and V_{OMI}(SP) for the 53 profiles where the same pixels from both data sets met the selection criteria. Data selection is based on profile locations, but the comparison is independent of the estimated in situ column amounts. The comparison should not be generalized to the entire SP and NRT products. However, it confirms that this subset of NRT and SP tropospheric columns is well correlated (r = 0.89). The slope and intercept are 1.74 (±0.13) and −0.79 (±0.10) × $10^{15}$$cm^{-2}$, respectively. The stratospheric column amounts for the two data sets, V_{OMI}^{strat}(NRT) and V_{OMI}^{strat}(SP), are compared in Figure 6b. Both the correlation (r = 0.88) and overall agreement between the two stratospheric data sets are good. On average, the NRT stratospheric column amounts in this sample of data are lower than the SP stratospheric columns by 0.09 × 10^{15} cm^{-2}. The implications of this result are discussed in section 5.3.

4.3. INTEX-B Averaging Kernel Analysis

[29] The effect of the NO_2 algorithms' a priori profiles on the comparisons with in situ measurements can be estimated using averaging kernels [*Eskes and Boersma*, 2003; *Boersma et al.*, 2005; *Schaub et al.*, 2006]. We apply this method in the present study by comparing the NO_2 column amounts, V_{OMI} and V_{in_situ} with the effective column amount, V_{eff}. The latter is the column OMI would retrieve if the in situ profile represented the vertical distribution of all tropospheric NO_2 in OMI's field of view, and if $m(z)$

Table 1. Air Mass Factors Computed From Measured and Model Profiles in Figures 3 and 4[a]

Campaign	Profile Type		
	Measured	Model 1	Model 2
INTEX-A: composite summer Atlantic Ocean (Figure 4a)	1.7	1.1	1.2
INTEX-A: composite winter continental (Figure 4b)	1.1	0.9	0.8
PAVE: composite winter continental (Figure 4c)	0.9	1.0	0.9
INTEX-B: southeastern U.S. (Figure 3a)	0.8	0.8	–
INTEX-B: Gulf of Mexico (Figure 3b)	1.0	1.2	–

[a]For the Atlantic composite, model 1 is a nearshore profile and model 2 is offshore. For the Continental composites, model 1 is from a rural region in Kansas and model 2 represents the urban area around Washington, DC. For the INTEX-B profiles, the model profile selected is the one nearest the measurement.

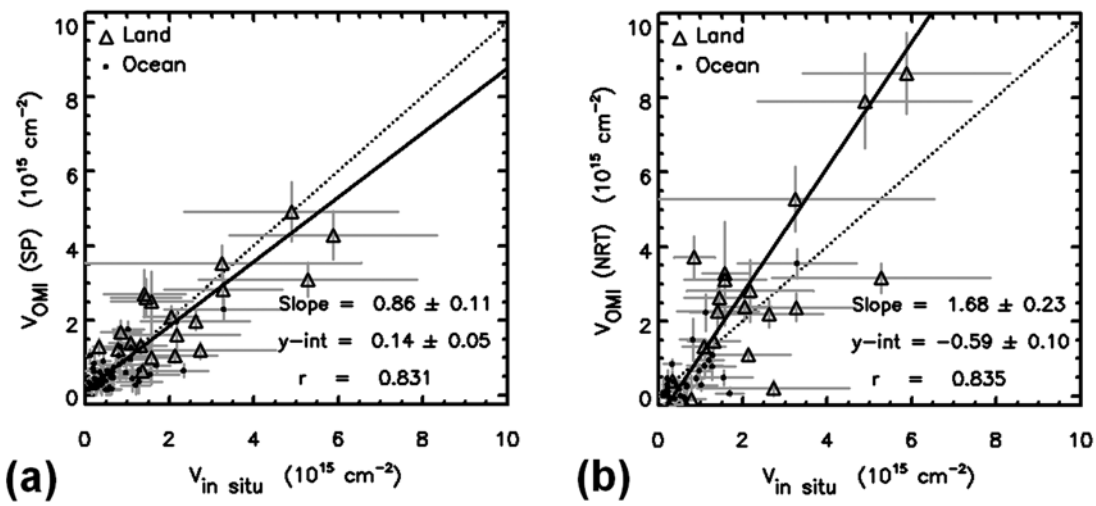

Figure 5. Comparisons of OMI tropospheric NO_2 retrievals with in situ columns from INTEX-B for the standard and near-real-time products (a) V_{OMI}(SP) versus V_{in_situ} and (b) V_{OMI}(NRT) versus V_{in_situ}, where V_{OMI} is OMI tropospheric NO_2 (SP or NRT) and V_{in_situ} is the integrated in situ column. Symbols indicate land measurements (triangle) or ocean measurements (dot). The dotted line is a 1:1 ratio, and the solid line is the fit to the data. Slope and intercept uncertainties shown do not account for potential systematic errors in the analysis (see text).

accurately characterized atmospheric scattering. We can write formal definitions of the three column amounts as

$$V_{OMI} = \frac{S_{OMI}}{M} \tag{3}$$

$$V_{in_situ} = \int_{zsurf}^{ztrop} \mathrm{d}z \cdot n_{in_situ}(z) \tag{4}$$

$$V_{eff} = \int_{zsurf}^{ztrop} \mathrm{d}z \cdot A(z) \cdot n_{in_situ}(z) \tag{5}$$

In these expressions, S_{OMI} is OMI's measured tropospheric slant column, and $n_{in_situ}(z)$ is the number density from the in situ profile. The quantity $A(z)$ is the OMI averaging kernel, which can be written as

$$A(z) = \frac{m(z)}{M} \tag{6}$$

where $m(z)$, and M are the same quantities in equation (1). The a priori quantities M, $m(z)$ and $A(z)$ are different in the SP and NRT algorithms. Thus the effective columns for the

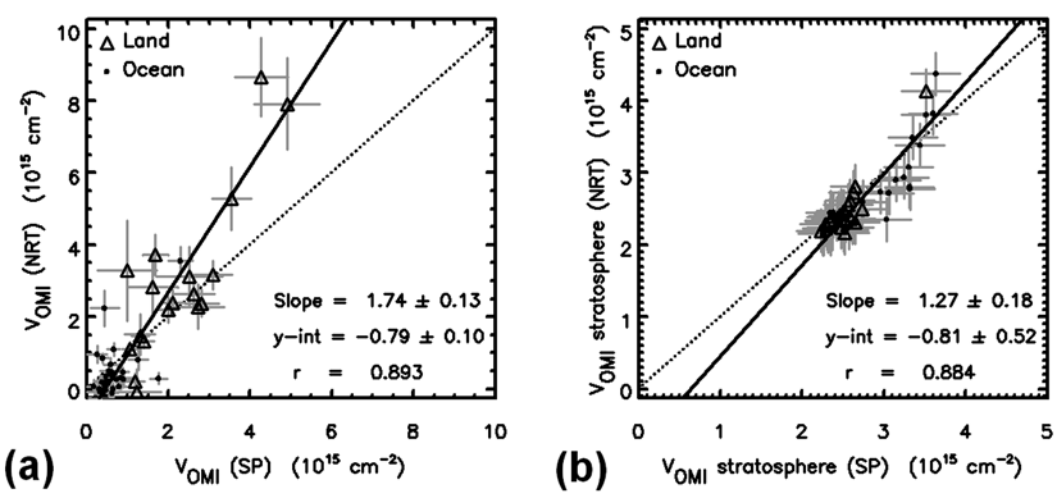

Figure 6. OMI standard product and near-real-time NO_2 retrievals. (a) Tropospheric columns V_{OMI}(NRT) versus V_{OMI}(SP) and (b) stratospheric columns V_{OMI}^{strat}(NRT) versus V_{OMI}^{strat}(SP). Symbols indicate land measurements (triangle) or ocean measurements (dot). The dotted line is a 1:1 ratio, and the solid line is the fit to the data. The data are based on a limited set of pixels near locations of INTEX-B measurements and are not intended for general comparisons of the two OMI products. Slope and intercept uncertainties shown do not account for potential systematic errors in the analysis (see text).

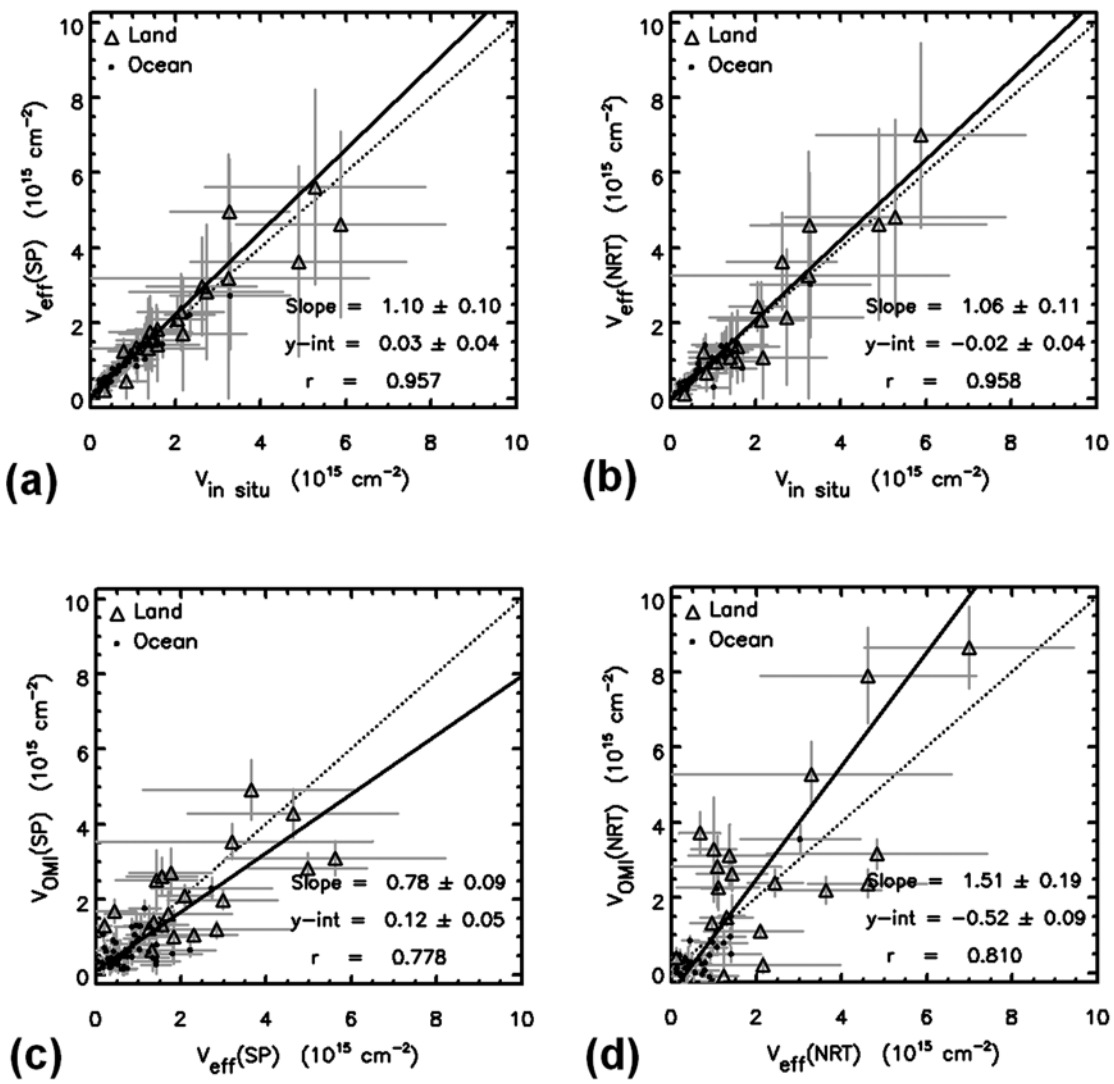

Figure 7. INTEX-B column comparisons (see text). (a) V_{eff}(SP) versus V_{in_situ}, (b) V_{eff}(NRT) versus V_{in_situ}, (c) V_{OMI}(SP) versus V_{eff}(SP), and (d) V_{OMI}(NRT) versus V_{eff}(SP), where V_{eff} is the integrated product of the in situ measurements and the OMI averaging kernel (SP or NRT). Symbols indicate land measurements (triangle) or ocean measurements (dot). The dotted line is a 1:1 ratio, and the solid line is the fit to the data. The slopes of the lines in Figures 7a and 7b are ratios of AMFs computed with in situ profiles to those computed with the algorithms' model profiles. The slopes in Figures 7c and 7d are ratios of OMI to in situ columns that would result if the OMI AMFs were computed with the in situ profiles, instead of the model profiles. Slope and intercept uncertainties shown do not account for potential systematic errors in the analysis (see text).

two algorithms are also different, and we write them as V_{eff}(SP) and V_{eff} (NRT), respectively.

[30] Figures 7a and 7b show the respective comparisons of V_{eff}(SP) and V_{eff}(NRT) with V_{in_situ}. From equations (1), (5) and (6), it is evident that the ratio of the y to x coordinates (V_{eff}/V_{in_situ}) is

$$\frac{y}{x} = \frac{\int_{zsurf}^{ztrop} dz \cdot m(z) \cdot [n_{in_situ}(z)/V_{in_situ}]}{\int_{zsurf}^{ztrop} dz \cdot m(z) \cdot [n_a(z)/V_a]}, \qquad (7)$$

which is the ratio of an AMF computed with the in situ profile, n_{in_situ} to one computed with the a priori profile, n_a. The y intercepts in Figures 7a and 7b are within 0.03×10^{15} cm^{-2} of the origin, and the correlation coefficients are 0.96. The slopes are 1.10 (±0.10) and 1.06 (±0.11) for the SP and NRT data, respectively. These slopes indicate that AMFs computed with the measured profiles are, on average, 10% and 6% larger than AMFs based on the a priori model profiles. However, the uncertainties make the slopes statistically equivalent to unity, so that the shapes of the algorithm's model profiles are effectively indistinguishable from those measured in INTEX-B.

[31] The quotient V_{OMI}/V_{eff} is the ratio of the tropospheric column OMI would retrieve if the algorithms' AMFs were computed from n_{in_situ} (rather than n_a) to the in situ column V_{in_situ}. Analysis similar to that used in deriving equation (7)

Table 2. Slopes and Intercepts From Linear Regression Analyses of V_{OMI}(SP) Versus V_{in_situ} and V_{OMI}(NRT) Versus V_{in_situ} (See Text)[a]

Method Number	Method	OMI Standard Product (n = 71), 10^{15} cm^{-2}				OMI NRT Product (n = 58), 10^{15} cm^{-2}			
		Slope	y Intercept	r	χ^2_r	Slope	y Intercept	r	χ^2_r
1	nominal	0.86 (±0.11)	0.14 (±0.05)	0.83	1.7	1.68 (±0.23)	−0.59 (±0.10)	0.83	2.0
2	bin mixing ratios using means	0.82 (±0.09)	0.15 (±0.04)	0.74	1.6	1.61 (±0.21)	−0.52 (±0.08)	0.70	2.3
3	extrapolate with scaled model	0.81 (±0.10)	0.15 (±0.04)	0.84	1.6	1.63 (±0.24)	−0.57 (±0.10)	0.82	2.0
4	extrapolate with a constant mixing ratio	0.89 (±0.11)	0.15 (±0.05)	0.80	2.0	2.03 (±0.28)	−0.71 (±0.11)	0.82	2.2
5	only columns with extrapolations < 40%	0.79 (±0.11)	0.17 (±0.05)	0.85	2.1	1.73 (±0.29)	−0.60 (±0.13)	0.82	2.5
6	only small columns (<1 × 10^{15} cm^{-2})	0.60 (±0.16)	0.21 (±0.06)	0.28	1.3	1.34 (±0.36)	−0.44 (±0.16)	0.19	2.2
7	only large columns (>1 × 10^{15} cm^{-2})	1.01 (±0.50)	0.22 (±0.98)	0.75	0.7	1.90 (±0.92)	−1.03 (±1.85)	0.78	0.6
8	cloud fraction < 10%, aerosol index < 1.0	0.90 (±0.17)	0.11 (±0.08)	0.90	1.1	1.48 (±0.41)	−0.46 (±0.24)	0.84	1.9
9	constant x, y errors (error = 1 × 10^{15} cm^{-2})	0.80 ± 0.14	0.13 ± 0.17	0.83	0.2	1.57 ± 0.22	−0.75 ± 0.30	0.83	0.4
10	reduced major axis (unweighted)	0.83 ± 0.08	0.10 ± 0.08	0.83	0.4	1.46 ± 0.12	−0.61 ± 0.14	0.83	2.8
11	force fitted line through the origin	1.10 ± 0.08	0.0	0.83	1.8	0.86 ± 0.07	0.0	0.83	3.0

[a]In each analysis, the number of data points is n, the Pearson's correlation coefficient is r, and the reduced chi square is χ^2_r.

gives this quotient, approximately equal to the slopes in Figures 7c and 7d, as

$$\frac{y}{x} = \frac{S_{OMI}}{\int_{zsurf}^{ztrop} dz \cdot m(z) \cdot n_{in_situ}(z)}, \tag{8}$$

Equation (8) is a means of comparing OMI measurements to in situ measurements independently of the a priori profile. The respective slopes for the SP and NRT data are 0.79 (±0.10) and 1.51 (±0.19). This result indicates that for moderate-to-large columns, the OMI SP underestimates tropospheric NO_2, while the NRT product overestimates it, when the effects of the a priori profiles are removed from both algorithms. The nonunity slopes in both cases imply errors in the tropospheric slant column, S_{OMI}, and/or the scattering weights, $m(z)$.

5. Discussion

[32] In this study, efforts were made to ensure that the linear regressions were robust with respect to the analysis, but aspects of the procedures warrant further discussion. We describe here a series of sensitivity tests conducted to evaluate the findings in this study. Results of these studies are summarized in Table 2, which gives slopes and intercepts of lines fitted to either V_{OMI}(SP) versus V_{in_situ} or to V_{OMI}(NRT) versus V_{in_situ} using varying analysis methods. With each method are shown the number of profiles, n, the correlation coefficient, r, and the reduced chi-square, χ^2_r.

5.1. Profile Analysis and Extrapolation Sensitivities

[33] The aircraft in situ mixing ratio measurements are of high quality and yield reliable column amounts in the range of pressure levels where measurements were made. However, because of flight restrictions, complete profiles in polluted areas, where NO_2 amounts are above the OMI detection limit, are rarely available. Polluted profiles often require large extrapolations and are less accurate. Satellite validation based on aircraft campaigns like INTEX-B require data selection that balances the accuracy of the in situ columns against need for measurements in a range of conditions.

[34] The first four entries in Table 2 indicate sensitivities of the results to the method of profile analysis. These tests used the full set of profiles for the SP and NRT data sets (71 and 58). Method 1 is the nominal approach described in section 3. Methods 2–4 are the same as method 1, except that method 2 uses means instead of medians to bin the raw mixing ratio data, method 3 extrapolates the lower part of the profiles based only on the scaled model profile, and method 4 extrapolates the lower part with a constant mixing ratio. Although the mean and median mixing ratios in some bins differed by an order of magnitude, the effect of binning choice on the final integrated column amount was usually small. When using means, a small number of integrated columns changed by a factor of ~2, and these profiles appeared as outliers in scatterplots (analogous to Figure 5) with correspondingly smaller correlation coefficients. Scatterplots based on median binning contained fewer such outliers. However, on average, the choice of binning method affected the slopes by less than 5%. Similarly, the effect of profile extrapolation method was also small. For example, using method 3 or 4 alone changed the slope by approximately ±5% for the SP data.

[35] The final values for the errors in the slopes and intercepts given in section 4.2 account for the random errors, the systematic uncertainties from methods 1–4, and an additional effect (5–10%) resulting from uncertainties in the OMI error estimates (see section 3.2). Tests of all combinations of these methods and OMI error assumptions yield slopes ranging from 0.73 to 1.02 for the SP data and 1.34 to 2.25 for the NRT data. Analogous ranges were determined for the intercepts. Combining all errors, we obtain the overall uncertainties in the respective slopes and intercepts of ±0.2 and ±0.1 × 10^{15} cm^{-2} for the SP data, and ±0.6 and ±0.2 × 10^{15} cm^{-2} for the NRT data.

5.2. Data Selection and Linear Regression Sensitivities

[36] Methods 5–8 test the sensitivities of the results to a variety of data selection criteria. Excluding profiles with top-plus-bottom extrapolations that are more than 40% of the total column (about 10–20 profiles) changed the slopes by approximately 8%. This change is statistically insignificant, implying that data with the largest extrapolations have a small effect on the regressions. Linear regressions involving only column amounts <10^{15} cm^{-2}, halves the number of available profiles and changes the fitted slopes by more than 20%. Selecting only columns >10^{15} cm^{-2} restricts the data sets to 18 points each, and yielded fitted slopes approxi-

mately 15% larger than their nominal values. A stricter cloud fraction limit of 10%, combined with screening for aerosol indices above the aerosol detection limit of 1.0 [*Torres et al.*, 2001] reduced the number of profiles by a factor of ~3. The slope for the SP data increased by 5% and the NRT slope decreased by 12%, while the diagnostics r and χ^2_r improved for both products. The resultant NRT slope of 1.48 (±0.41) is consistent with the slope of 1.4 obtained by *Boersma et al.* [2008b] in their fit to a subset of 21 profiles from the March phase of INTEX-B.

[37] In this study we use a least squares approach, with data weighted by errors in both x and y coordinates, as described in section 4.2. Results of other fitting approaches are shown in methods 9–11. To estimate the effect of the weighting, we performed two unweighted fits. In the first, we assigned fixed error bars of 10^{15} cm^{-2} to all column measurements. The resultant slopes are 7% lower than the nominal values, which is within the range of their uncertainties. The second test is an unweighted reduced major axis (RMA) approach [*Hirsch and Gilroy*, 1984], as used by *Boersma et al.* [2008b] in their INTEX-B/OMI analysis and by *Martin et al.* [2006] in their comparisons of aircraft and SCIAMACHY data. Results from the unweighted RMA analysis, using all of the data in this study, yielded a slope of 0.83 (±0.08) for the SP data and 1.46 (±0.12) for the NRT data. For the complete set of profiles analyzed in the present study, differences between the weighted and unweighted fits are small, due in part to the large size and good correlation ($r > 0.8$) of the data set. However, in some cases unweighted approaches can be disproportionately sensitive to individual measurements. As an example, a column measurement with a 50% uncertainty was found to have little effect on weighted regressions involving all 71 data points. Changing its column value by an amount consistent with its uncertainty affected the slope in a weighted fit by approximately 2%. In an unweighted fit, a change in this single data point affected the slope by >12%. Larger effects were seen on fits when only small subsets of the 71 data points were included.

[38] As a final test (method 11), we performed regressions in which the fitted line was forced through the origin. The SP and NRT analyses yielded slopes of 1.1 and 0.9, respectively, indicating good "average" agreement between the OMI and in situ measurements. However, the chi-square is significantly increased in the NRT analysis, since it forces the large y intercept to zero.

5.3. Differences Among the Measurements

[39] In section 4, a comparison between the two OMI tropospheric columns, V_{OMI}(NRT) and V_{OMI}(SP), presented. Sensitivity studies were conducted (section 5.2) using stricter cloud and aerosol screening, exclusion of columns $<10^{15}$ cm^{-2} and unweighted fits. In all cases, the slopes were within 15% of the nominal value, and the y intercepts varied between -0.6 and -1.0×10^{15} cm^{-2}. When the fitted line is forced through the origin, the slope is close to unity, implying good "average" agreement between V_{OMI}(NRT) and V_{OMI}(SP) for all column amounts, but with a larger chi-square. Here we examine reasons for the differences between the two OMI products as well as the differences relative to the INTEX-B measurements.

[40] The tropospheric slant column, S_{OMI}, is one possible cause of the disparities. Figure 6a indicates that NRT tropospheric columns are generally larger than corresponding SP columns. We explore the possibility that this discrepancy results from differences between the NRT and SP tropospheric slant columns S_{OMI}(NRT) and S_{OMI}(SP), respectively. Both the NRT and SP algorithms compute a tropospheric slant column by subtracting the estimated stratospheric slant column, S^{strat}_{OMI}(NRT) or S^{strat}_{OMI}(SP), from the total slant column. The total slant column, S^{total}_{OMI}, and the stratospheric air mass factors M^{strat} are the same in both algorithms. Given that the stratospheric vertical column, V^{strat}_{OMI}(NRT) or V^{strat}_{OMI}(SP), is related to the stratospheric slant column by an equation analogous to equation (3), the difference between the derived tropospheric slant columns can be written

$$[S_{OMI}(\mathrm{NRT}) - S_{OMI}(\mathrm{SP})] = M^{strat} \cdot \left[V^{strat}_{OMI}(\mathrm{SP}) - V^{strat}_{OMI}(\mathrm{NRT})\right] \tag{9}$$

[41] The average difference V^{strat}_{OMI}(SP) − V^{strat}_{OMI}(NRT) for the data examined in this study is approximately 0.1×10^{15} cm^{-2}. Thus, for a typical stratospheric AMF of $M^{strat} = 3$, equation (9) implies a corresponding difference, S_{OMI}(NRT) − S_{OMI}(SP), of about 0.3×10^{15} cm^{-2}. Under polluted conditions, tropospheric air mass factors, M, are approximately unity, so that using equation (3), the tropospheric vertical column difference, V_{OMI}(NRT) − V_{OMI}(SP), would also be $\sim 0.3 \times 10^{15}$ cm^{-2}. This difference is smaller than the discrepancies seen in Figure 6a for large vertical column amounts. These results imply that it is unlikely that stratospheric slant column differences account for the discrepancies between the two OMI tropospheric products for the several dozen points examined in this study.

[42] Slant columns might, nonetheless, be the source of differences between OMI and the in situ measurements or between the two OMI products at other times and locations. Preliminary examination of global NRT and SP data on other days shows stratospheric vertical column differences of 1×10^{15} cm^{-2} over continental-scale regions. Such stratospheric discrepancies would lead to even larger discrepancies in tropospheric vertical columns due to the tropospheric AMF scaling. However, these differences would be relatively small for analyses that include only large tropospheric vertical columns in highly polluted regions, where the stratosphere is a small fraction of the total column. The relatively simple wave-2 analysis used to estimate the stratosphere in the SP algorithm has been shown to be accurate on a global scale, yielding stratospheric residuals on the order of 0.2×10^{15} cm^{-2}, but regional differences between the modeled and actual stratosphere may be larger on some days [*Bucsela et al.*, 2006]. The cross-track anomaly in the OMI slant columns is largely corrected after spectral fitting and so is unlikely to affect the tropospheric vertical columns. However, the correction process, itself, may introduce an unknown bias in the total slant column amounts. Such a bias is an additive global constant for a given day. As such, it could potentially affect the stratospheric vertical columns, but would be unlikely to change the retrieved tropospheric VCDs.

[43] The other major source of error is the tropospheric AMF, which is dependent on the a priori NO_2 profile and the scattering weights, $m(z)$. We have shown that the NO_2 profiles affect the difference among the data sets in this study by less than 10%. The scattering weights are computed by radiative transfer, and depend on factors including surface pressure, albedo and the effects of clouds and aerosols. The surface pressures are a potential cause of differences between the two algorithms, since the NRT uses coarsely gridded real-time meteorological data, while the SP employs a high-resolution database of climatological means. Surface pressure differences can have a modest effect on the AMF, and a larger effect on profile extrapolation [*Boersma et al.*, 2008b]. The latter, of course, does not affect the direct NRT–SP comparison. The albedo differences between the two algorithms (which can be >0.02) are likely to make a significant contribution to the discrepancies between the retrievals. The remaining factors in the computation of the scattering weight are clouds and aerosols. Both are particularly difficult to parameterize in radiative transfer calculations. Neither algorithm explicitly accounts for aerosols, but on the basis of the analysis of *Martin et al.* [2003] we estimate aerosols to be relatively unimportant for the cases examined in this study. A comprehensive look at the OMI NRT and SP data and the effects of pressure, albedo, cloud and aerosols is beyond the scope of this study. However, initial comparisons of tropospheric VCDs reveal complex differences that vary in sign and magnitude over time and geographic region.

5.4. Other Validations

[44] *Boersma et al.* [2008b] have performed a separate analysis of INTEX-B data and compared them to the OMI NRT product. They used data from the March phase of the campaign, which covered the Gulf of Mexico and adjacent land areas, including Mexico City. The number of profiles in their study varied from 12 to 21, depending on the restrictions they imposed regarding data location, clouds, aerosols and profile extrapolation. As noted, some of their findings are consistent with the present study. However, given their smaller data set and differences in data quality, extrapolation technique and linear regression approach, a direct comparison of their results to those presented here is difficult.

[45] *Celarier et al.* [2008] have summarized comparisons of data from a number of validation experiments with tropospheric NO_2 from the OMI standard product. Ground-based zenith sky measurements from SAOZ are slightly lower than OMI with an average difference (SAOZ – OMI) of $\sim 0.3 \times 10^{15}$ cm^{-2}. Larger differences and more variability are seen in the tropospheric validations, which have been made with a variety of instruments and locations. MAX-DOAS measurements made in Europe during spring and summer 2005 correlate poorly with OMI tropospheric NO_2 data. For OMI versus MAX-DOAS regressions, correlation coefficients are between $r = 0.45$ and $r = 0.65$, and fitted line slopes range from 0.52 to 0.85. MF-DOAS measurements of tropospheric NO_2 obtained during INTEX-B from the Pacific Northwest National Laboratory in Richland, Washington are better correlated with SP data. The correlation coefficient is $r = 0.92$ and the slope is 0.81 (±11) for OMI versus MF-DOAS. This slope is slightly smaller than the value of 0.86 (±0.2) found in this study, but consistent within the bounds of uncertainty.

[46] Satellite comparisons with OMI can provide much greater temporal and spatial coverage than ground-based validations. However, data from GOME and SCIAMACHY each present their own unique challenges for use in validation. For example, the areal coverage of a GOME pixel is larger than OMI's by more than an order of magnitude. Furthermore, both satellites have overpass times much earlier than OMI, (local equator crossing time is 1030 for GOME and 1000 for SCIAMACHY, compared to 1340 for OMI). Such differences make comparisons difficult because of diurnal cycles in both sources and photochemistry of NO_2. *Boersma et al.* [2008a] have demonstrated that differences between the NRT product and SCIAMACHY data may be largely explained by diurnal NO_2 variation between observation times.

6. Summary and Conclusions

[47] We have examined in situ aircraft measurements of tropospheric NO_2 from UC Berkeley and compared them to OMI NO_2 from both the SP and NRT algorithms. In situ profiles from INTEX-A and PAVE have shapes that are qualitatively similar to those of GEOS-Chem model profiles used in the OMI SP algorithm. Average air mass factors computed from INTEX-B in situ profiles are slightly larger than AMFs from the GEOS-Chem and TM4 models used in the SP and NRT algorithms, respectively. Regressions of in situ versus model AMFs for all profiles in this study yield a slope 1.10 (±0.10) for the SP algorithm and a slope of 1.06 (±0.11) for the NRT algorithm. Improved time-dependent profiles are planned for implementation in future versions of the SP, algorithm, and these profiles may reduce some of the differences in the AMFs.

[48] We conducted a three-way comparison between the integrated in situ columns from INTEX-B and the two OMI products. The in situ columns are somewhat larger than columns from the OMI SP algorithm, as indicated by the slope of 0.86 (±0.2) and intercept of 0.14 (±0.1) $\times$ 10^{15} cm^{-2} for V_{OMI}(SP) versus V_{in_situ}. The Pearson's correlation coefficient is $r = 0.83$ for both products. These results have been shown to be robust with respect to the choices of profile binning and extrapolation explored in this study as well as assumptions about data errors. The slope and intercept for V_{OMI}(NRT) versus V_{in_situ} show a greater difference between those two data sets, although the correlation coefficient is approximately the same. In general the NRT results in this study were found to be somewhat more sensitive to analysis assumptions. Averaging kernel analysis implies that the shapes of the a priori profiles used in the two OMI algorithms make a relatively small contribution to these discrepancies. The direct comparison of V_{OMI}(NRT) and V_{OMI}(SP), using OMI data sampled in the vicinity of the INTEX-B profile measurements yields a high correlation coefficient $r = 0.89$. The comparison shows also that, for this limited subset of the OMI data, the SP and NRT algorithms produce significantly different tropospheric NO_2 amounts. Calculations suggest that the differences in the stratospheric field estimates between the algorithms are

not a major cause of the tropospheric discrepancies for these data. Other possibilities include surface pressure, albedo, and the effects of clouds and aerosols. Future work should help to quantify the similarities and differences between the two OMI algorithms and also lead to improved validation of OMI.

[49] **Acknowledgments.** Funding for this work is provided by the NASA Tropospheric Chemistry program. We thank the University of California Berkeley Department of Chemistry for the aircraft data and the KNMI TEMIS and NASA GSFC SIPS teams, respectively, for the NRT and standard product OMI data. We also appreciate the reviewers' comments, which were very helpful in improving this manuscript.

References

Acarreta, J. R., J. F. deHaan, and P. Stammes (2004), Cloud pressure retrieval using the O_2-O_2 absorption band at 477 nm, *J. Geophys. Res.*, *109*, D05204, doi:10.1029/2003JD003915.

Bey, I., D. J. Jacob, R. M. Yantosca, J. A. Logan, B. D. Field, A. M. Fiore, Q. Li, H. Y. Liu, L. J. Mickley, and M. G. Schultz (2001), Global modeling of tropospheric chemistry with assimilated meteorology: Model description and evaluation, *J. Geophys. Res.*, *106*, 23,073–23,096, doi:10.1029/2001JD000807.

Boersma, K. F., H. J. Eskes, and E. J. Brinksma (2004), Error analysis for tropospheric NO_2 retrieval from space, *J. Geophys. Res.*, *109*, D04311, doi:10.1029/2003JD003962.

Boersma, K. F., H. J. Eskes, E. W. Meijer, and H. M. Kelder (2005), Estimates of lightning NO_x production from GOME satellite observations, *Atmos. Chem. Phys.*, *5*, 2311–2331.

Boersma, K. F., et al. (2007), Near-real time retrieval of tropospheric NO_2 from OMI, *Atmos. Chem. Phys.*, *7*, 2103–2118.

Boersma, K. F., D. J. Jacob, H. J. Eskes, R. W. Pinder, J. Wang, and R. J. van der A (2008a), Intercomparison of SCIAMACHY and OMI tropospheric NO_2 columns: Observing the diurnal evolution of chemistry and emissions from space, *J. Geophys. Res.*, doi:10.1029/2007JD008816, in press.

Boersma, K. F., et al. (2008b), Validation of OMI tropospheric NO_2 observations during INTEX-B and application to constrain NO_x emissions over the eastern United States and Mexico, *Atmos. Environ.*, doi:10.1016/j.atmosenv.2008.02.004, in press.

Bucsela, E., E. Celarier, M. Wenig, J. Gleason, P. Veefkind, K. F. Boersma, and E. Brinksma (2006), Algorithm for NO_2 vertical column retrieval from the Ozone Monitoring Instrument, *IEEE Trans. Geosci. Remote Sens.*, *44*, 1245–1258.

Celarier, E. A., et al. (2008), Overview of the validation of nitrogen dioxide retrieved from the Ozone Monitoring Instrument, *J. Geophys. Res.*, *113*, D15S15, doi:10.1029/2007JD008908.

Chameides, W. L., and J. C. G. Walker (1973), Photochemical theory of tropospheric ozone, *J. Geophys. Res.*, *78*(36), 8751, doi:10.1029/JC078i036p08751.

Cleary, P. A., P. J. Wooldridge, and R. C. Cohen (2002), Laser-induced fluorescence detection of atmospheric NO_2 with a commercial diode laser and a supersonic expansion, *Appl. Opt.*, *41*(33), 6950–6956, doi:10.1364/AO.41.006950.

Crutzen, P. J. (1970), The influence of nitrogen oxides on the atmospheric ozone content, *Q. J. R. Meteorol. Soc.*, *96*, 320–325, doi:10.1002/qj.49709640815.

DeCaria, A. J., K. E. Pickering, G. L. Stenchikov, and L. E. Ott (2005), Lightning-generated NO_x and its impact on tropospheric ozone production: A three-dimensional modeling study of a Stratosphere-Troposphere Experiment: Radiation, Aerosols and Ozone (STERAO-A) thunderstorm, *J. Geophys. Res.*, *110*, D14303, doi:10.1029/2004JD005556.

Eskes, H. J., and K. F. Boersma (2003), Averaging kernels for DOAS total-column satellite retrievals, *Atmos. Chem. Phys.*, *3*, 1285–1291.

Heland, J., H. Schlager, A. Richter, and J. P. Burrows (2002), First comparison of tropospheric NO_2 column densities retrieved from GOME measurements and in situ aircraft profile measurements, *Geophys. Res. Lett.*, *29*(20), 1983, doi:10.1029/2002GL015528.

Herman, J. R., and E. A. Celarier (1997), Earth surface reflectivity climatology at 340 nm to 380 nm from TOMS data, *J. Geophys. Res.*, *102*(D23), 28,003–28,011, doi:10.1029/97JD02074.

Heue, K.-P., A. Richter, M. Bruns, J. P. Burows, C. von Friedeburg, U. Platt, U. Pundt, P. Wang, and T. Wagner (2005), Validation of SCIAMACHY tropospheric NO_2-columns with AMAXDOAS measurements, *Atmos. Chem. Phys.*, *5*, 1039–1051.

Hirsch, R. M., and E. J. Gilroy (1984), Methods of fitting a straight line to data: Examples in water resources, *Water Resour. Bull.*, *20*, 705–711.

Hudman, R. C., et al. (2005), A multi-platform analysis of the North American reactive nitrogen budget during the ICARTT summer intensive, *Eos Trans. AGU*, *86*(52), Fall Meet. Suppl., A54C-02.

Koelemeijer, R. B. A., J. F. De Haan, and P. Stammes (2003), A database of spectral surface reflectivity in the range 335–772 nm derived from 5.5 years of GOME observations, *J. Geophys. Res.*, *108*(D2), 4070, doi:10.1029/2002JD002429.

Levelt, P. F., E. Hilsenrath, G. W. Leppelmeier, G. B. J. van den Oord, P. K. Bhartia, J. Tamminen, J. F. de Haan, and J. P. Veefkind (2006), Science objectives of the Ozone Monitoring Instrument, *IEEE Trans. Geosci. Remote Sens.*, *44*, 1199–1208, doi:10.1109/TGRS.2006.872336.

Liu, S. C., M. Trainer, F. C. Fehsenfeld, D. D. Parrish, E. J. Williams, D. W. Fahey, G. Heubler, and P. C. Murphy (1987), Ozone production in the rural troposphere and the implications for regional and global ozone distributions, *J. Geophys. Res.*, *92*, 4191–4207, doi:10.1029/JD092iD04p04191.

Martin, R. V., et al. (2002a), An improved retrieval of tropospheric nitrogen dioxide from GOME, *J. Geophys. Res.*, *107*(D20), 4437, doi:10.1029/2001JD001027.

Martin, R. V., et al. (2002b), Interpretation of TOMS observations of tropical tropospheric ozone with a global model and in situ observations, *J. Geophys. Res.*, *107*(D18), 4351, doi:10.1029/2001JD001480.

Martin, R. V., D. J. Jacob, K. Chance, T. P. Kurosu, P. I. Palmer, and M. J. Evans (2003), Global inventory of nitrogen oxide emissions constrained by space-based observations of NO_2 columns, *J. Geophys. Res.*, *108*(D17), 4537, doi:10.1029/2003JD003453.

Martin, R. V., C. E. Sioris, K. V. Chance, T. B. Ryerson, T. H. Bertram, P. J. Woolridge, R. C. Cohen, J. A. Neuman, A. Swanson, and F. M. Flocke (2006), Evaluation of space-based constraints on nitrogen oxide emissions with regional aircraft measurements over and downwind of eastern North America, *J. Geophys. Res.*, *111*, D23S60, doi:10.1029/2006JD007530.

Murphy, D., D. Fahey, M. Proffitt, S. Liu, C. Eubank, S. Kawa, and K. Kelly (1993), Reactive odd nitrogen and its correlation with ozone in the lower stratosphere and upper troposphere, *J. Geophys. Res.*, *98*, 8751–8773, doi:10.1029/92JD00681.

Palmer, P. I., D. J. Jacob, K. Chance, R. V. Martin, R. J. D. Spurr, T. P. Kurosu, I. Bey, R. Yantosca, and A. Fiore (2001), Air mass factor formulation for spectroscopic measurements from satellites: Application to formaldehyde retrievals from the Global Ozone Monitoring Experiment, *J. Geophys. Res.*, *106*, 14,539–14,550, doi:10.1029/2000JD900772.

Penner, J. E., C. S. Atherton, J. Dignon, S. J. Ghan, J. J. Walton, and S. Hameed (1991), Tropospheric nitrogen: A three-dimensional study of sources, distributions, and deposition, *J. Geophys. Res.*, *96*, 959–990, doi:10.1029/90JD02228.

Pickering, K. E., A. M. Thompson, R. R. Dickerson, W. T. Luke, D. P. McNamara, J. Greenberg, and P. R. Zimmerman (1990), Model calculations of tropospheric ozone production potential following observed convective events, *J. Geophys. Res.*, *95*, 14,049–14,062, doi:10.1029/JD095iD09p14049.

Press, W. H., B. P. Flannery, S. A. Teukolsky, and W. T. Vetterling (1992), *Numerical Recipes: The Art of Scientific Computing*, Cambridge Univ. Press, New York.

Ridley, B. A., J. E. Dye, J. G. Walega, J. Zheng, F. E. Grahek, and W. Rison (1996), On the production of active nitrogen by thunderstorms over New Mexico, *J. Geophys. Res.*, *101*, 20,985–21,005, doi:10.1029/96JD01706.

Schaub, D., K. F. Boersma, J. W. Kaiser, A. K. Weiss, D. Folini, H. J. Eskes, and B. Buchmann (2006), Comparison of GOME tropospheric NO_2 columns with NO_2 profiles deduced from ground-based in situ measurements, *Atmos. Chem. Phys.*, *6*, 3211–3229.

Seinfeld, J. H., and S. N. Pandis (1998), *Atmospheric Chemistry and Physics: From Air Pollution to Climate Change*, John Wiley, New York.

Thornton, J. A., P. J. Wooldridge, and R. C. Cohen (2000), Atmospheric NO_2: In situ laser-induced fluorescence detection at parts per trillion mixing ratios, *Anal. Chem.*, *72*, 528–539, doi:10.1021/ac9908905.

Thornton, J. A., P. J. Wooldridge, R. C. Cohen, E. J. Williams, D. Hereid, F. C. Fehsenfeld, J. Stutz, and B. Alicke (2003), Comparisons of in situ and long path measurements of NO in urban plumes, *J. Geophys. Res.*, *108*(D16), 4496, doi:10.1029/2003JD003559.

Torres, O., R. Decae, P. Veefkind, and G. de Leeuw (2001), OMI aerosol retrieval algorithm, in *OMI-EOS Algorithm Theoretical Basis Document*, chap. 4, pp. 1–24, R. Neth. Meteorol. Inst., De Bilt, Netherlands.

van Noije, T. P. C., et al. (2006), Multi-model ensemble simulations of tropospheric NO_2 compared with GOME satellite retrievals for the year 2000, *Atmos. Chem. Phys.*, *6*, 2943–2979.

Wenig, M. O., A. M. Cede, E. J. Bucsela, E. A. Celarier, K. F. Boersma, J. P. Veefkind, E. J. Brinksma, J. F. Gleason, and J. R. Herman (2008), Validation of OMI tropospheric NO_2 column densities using direct-sun mode Brewer measurements at NASA Goddard Space Flight Center, *J. Geophys. Res.*, doi:10.1029/2007JD008988, in press.

T. H. Bertram, R. C. Cohen, A. E. Perring, and P. J. Wooldridge, Department of Chemistry, University of California, Berkeley, CA 94720, USA.

K. F. Boersma, R. Dirksen, and J. P. Veefkind, Royal Netherlands Meteorological Institute, NL-3730 AE De Bilt, Netherlands.

E. J. Bucsela, SRI International, Menlo Park, CA 94025, USA. (bucsela@ix.netcom.com)

E. A. Celarier, SGT, Inc., 7701 Greenbelt Road, Suite 400, Greenbelt, MD 20770, USA.

J. F. Gleason, NASA Goddard Space Flight Center, Code 613.3, Greenbelt, MD 20771, USA.

M. O. Wenig, Department of Physics and Materials Science, City University of Hong Kong, Kowloon, Hong Kong.